Advanced Optical Materials

ADVANCED OPTICAL MATERIALS
www.advopticalmat.de

RESEARCH ARTICLE OPEN ACCESS

Non-Volatile Silicon Mach-Zehnder Switches with 0.7 π Phase Shift Based on Graphene Heaters and Sb_2Se_3 Phase Change Material

Jens Samland[1] | Felix Hoff[2] | Timo Veslin[2] | Holger Lerch[1] | Bartos Chmielak[1] | Martin Otto[1] | Caroline Porschatis[1] | Bárbara Canto[1] | Stephan Suckow[1] | Matthias Wuttig[2,3] | Max C. Lemme[1,4]

[1]AMO GmbH, Aachen, Germany | [2]I. Institute of Physics (IA) RWTH Aachen University, Aachen, Germany | [3]Peter-Grünberg-Institute – JARA-Institute Energy Efficient Information Technology, Wilhelm-Johnen-Straße, Jülich, Germany | [4]Chair of Electronic Devices, RWTH Aachen University, Aachen, Germany

Correspondence: Max C. Lemme (max.lemme@eld.rwth-aachen.de)

Received: 8 October 2025 | **Revised:** 29 April 2026 | **Accepted:** 8 June 2026

Keywords: graphene micro heaters | integrated photonics | non-volatile Mach-Zehnder switch | phase change material Sb_2Se_3

ABSTRACT

Photonic integrated circuits (PICs) can deliver unparalleled performance for future neuromorphic computing applications. Such neuromorphic PICs require a large number of tunable switches, which are typically realized with current-controlled heaters, resulting in considerable energy consumption. Non-volatile photonic devices based on phase change materials (PCMs) can overcome this challenge, promising zero power consumption during operation. In this work, we experimentally demonstrate non-volatile Mach-Zehnder switches (MZI) utilizing the phase change material antimony triselenide (Sb_2Se_3). The PCMs are controllably switched with graphene heaters from the amorphous to the crystalline state. This leads to a π-shift of 0.7, a $V_\pi L \approx 0.56$ Vcm, and a shift per micrometer of Sb_2Se_3 of 0.014 π/µm, and a high extinction ratio of 28 dB. Additionally, we perform state-of-the-art simulations to predict the temperature in the devices and to support our measurements. The data demonstrates that switches based on graphene heaters and Sb_2Se_3 are suitable for achieving large phase shifts while avoiding high thermal budgets as for doped silicon heaters. Moreover, our devices were fabricated on wafer-scale enabling scalability of the fabrication process in the future as it is beneficial for advanced applications like neuromorphic computing, integrated optical memory, tunable filter arrays and delay lines with permanent trimming and optical FPGAs based on phase change materials.

1 | Introduction

Phase change materials enable non-volatile switching devices for electronic and integrated photonic circuits (PICs) [1–4]. The latter enables the design of Mach-Zehnder interferometers (MZI) that operate without permanent heaters, i.e., they only consume electrical power during switching events. Emerging fields such as neuromorphic photonic computing [5, 6] for artificial intelligence applications [7, 8], integrated optical memory [9], tunable filter arrays and delay lines with permanent trimming [10] and optical FPGAs based on phase change materials [11] could particularly benefit from such non-volatile switches. Neural networks consist of multiple layers with adjustable weights. In neuromorphic photonic networks, these weights can be realized using the phase of the optical signal, for example, by controlling the temperature of MZIs. In large networks, the electrical power required for heating is considerable. Additionally, heat dissipation can be problematic, leading to signal crosstalk. A neural network with weights based on non-volatile switches could overcome these challenges and achieve zero power consumption once it is trained.

The prototype phase change material germanium antimony telluride ($Ge_2Sb_2Te_5$, or GST) has been studied in combination with photonics for non-volatile integrated devices [12–15]. However, GST exhibits significant optical absorption losses in the crystalline state for visible and telecommunication wavelengths. In contrast, antimony triselenide (Sb_2S_3) is a low absorption loss alternative with a large bandgap of approximately 1.6 to 1.8 and 2.2 to 2.8 eV in the crystalline and amorphous phases, respectively [16–19]. It remains transparent to light with a wavelength of approximately 600 nm in the amorphous phase. It has been incorporated into photonic devices in the literature [19–22]. Sb_2Se_3 offers a reasonable index contrast of $\Delta n \approx 0.76$ between the amorphous and crystalline phases at the standard telecommunication wavelength of 1550 nm [22] and exhibits low losses ($k < 10^{-5}$) [23–25]. Moreover, Sb_2Se_3 exhibits better morphological stability upon switching, and higher chemical stability compared to Sb_2S_3. To date, a programmable multimode interference coupler and Mach-Zehnder switch utilizing Sb_2Se_3 have been reported, where the PCM was switched with a focused laser beam [26]. In contrast, Ríos et al. [27]. and Fang et al. [28]. switched Sb_2Se_3 on photonic waveguides using a doped silicon microheater integrated on the PIC chip. Ríos et al. [29]. compared the switching behavior between GST and Sb_2Se_3 with graphene microheaters, but without photonics, and Fang et al. [30]. demonstrated the concept with a photonic micro ring resonator. Notably, the fabrication of graphene devices [31, 32] does not require high thermal budgets, unlike doped silicon heaters, which require ion implantation and annealing. This is a decisive advantage for future electronic-photonic systems, where PICs may be integrated in the back-end-of-the-line (BEOL) of advanced silicon logic chips, which limits processing temperatures to approximately 400 °C.

Here, we experimentally demonstrate non-volatile MZI switches based on graphene heaters and Sb_2Se_3. We discuss our choice of the PCM Sb_2Se_3 in more detail in the SI. Our MZIs show a large tuning range and high extinction ratio compared to previous experiments with graphene heaters. Both features are essential for using such switches in future, for example in photonic networks for photonic computing.

2 | Methods

2.1 | Experimental Setup

The photonic waveguides were fabricated on 150 mm silicon on insulator (SOI) wafers with a 220 nm thick top silicon layer and a 3 µm thick buried oxide (BOX). The photonic layer included waveguides, multimode interference couplers (MMIs), MZIs, and grating couplers. The waveguides had a height of $h_{WG} = 220$ nm and a width of $w_{WG} = 500$ nm. The 2 × 2 MMIs had a width of $w_{MMI} = 8.5$ µm and a length of $L_{MMI} = 86$ µm. The MZIs had a lower arm length of $L = 1500$ µm and a path length difference between the two arms of $\Delta L = 40$ µm. The grating couplers had a period of 630 nm, a 50% filling factor, and an etch depth of 70 nm. The photonic layer was covered with a 250 nm thick silicon dioxide (SiO_2) cladding with low-pressure chemical vapor deposition (LPCVD) and planarization. This provided a smooth surface for the graphene heaters. The latter were fabricated on top of the cladding and had a length of $L_{Graph} = 90$ µm and a width of $w_{Graph} = 20$ µm. Details of the fabrication process of the photonic layer and the graphene heater can be found in the Ref [33]. Finally, 42.9 nm of the amorphous phase change material Sb_2Se_3 was grown via magnetron sputter deposition on top of the Al_2O_3 passivation layer. A 15.1 nm zinc sulfide (ZnS):SiO_2 layer was subsequently added to prevent oxidation of the PCM layer. The final thickness of both layers was determined using X-ray reflectometry (XRR), see Figure S1 in the appendix. The structuring of this layer was accomplished through a lift-off process. The PCM had final dimensions of $L_{PCM} = w_{PCM} = 50$ µm. A schematic of a device is shown in Figure 1a, with the photonic layer shown in red. A microscope image is shown in Figure 1b. A schematic cross-section of the MZI with key dimensions is shown in Figure 2a.

2.2 | Simulation

We used the Lumerical HEAT + FDE software package to model the fabricated structures shown in Figure 2a. Specifically, we aimed to predict the temperature T at the position of the PCM as a function of the dissipated power of the heater P_E, because we cannot measure the temperature directly on-chip. Instead, we utilized the relationship between the temperature change ΔT in an MZI arm and the resulting measurable phase shift $\Delta\varphi$ in the MZI output to compare measurements and simulations at the MZI arm position. By demonstrating that the temperature increase and phase shift can be accurately predicted at this position, we can then simulate the temperature at the PCM position, which should be close to the actual temperature in the device. The relationship reads

$$\Delta\varphi = \frac{2\pi}{\lambda} \cdot L \cdot \frac{\partial n}{\partial T} \cdot \Delta T \tag{1}$$

Here, λ is the wavelength, L is the length over which the MZI arm is heated, $\partial n/\partial T$ is the thermal coefficient, which is $1.86 \bullet 10^{-4}$ K^{-1} for silicon, and $\Delta T = T—T_{R,}$ where T_R is the room temperature. First, we simulated $\Delta\varphi$ as a function of ΔT and P_E, incorporating the contact (R_c) and sheet (R_{sh}) resistances of the graphene, including their respective uncertainties (Figure 2b, blue shadow area). R_c and R_{sh} are required to compare the simulation to the measured data. While the power P_E was dissipated across the entire heating structure in the experiment, it was dissipated only along the designed length of the graphene heater L_{graph} in the simulation (compare Figure 1b). We extracted values of $R_c = 10.4 \pm 1.4$ kΩ and $R_{sh} = 3803 \pm 127$ Ω/□ by applying the transfer length method (TLM). Such wide ranges are typical for graphene TLM structures, and can be attributed to the non-uniform distribution of grain boundaries, wrinkles and other defects in CVD graphene [34, 35] or resist residues from the transfer process [36, 37]. Additionally, the carrier density in graphene affects the contact resistance, which can even cause negative values in the extraction process [38–45]. With the extracted values, we deduced that 41% of the measured power P_E was dissipated across the straight part of the heater (L_{graph}). Next, we experimentally determined $\Delta\varphi$ as a function of P_E from the measured shift in the optical transmission spectrum (Figure 2b, blue squares). The data points were fitted linearly (Figure 2b, blue dashed line). The experimental (blue squares) and simulation data (blue shadow

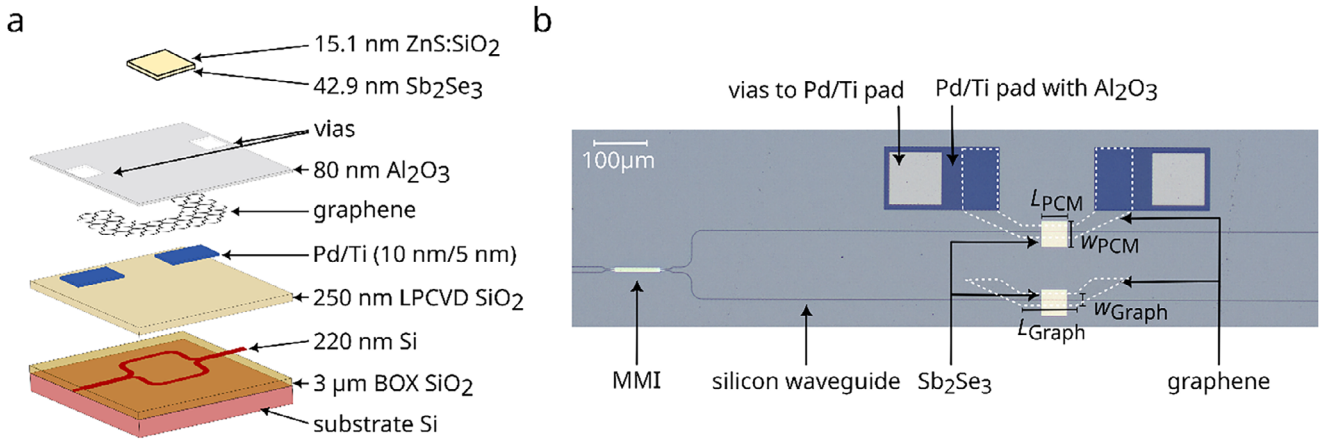

FIGURE 1 | PIC and device layout. (a) The photonic layers consist of 220 nm silicon waveguides on a 3 µm thick buried oxide (BOX). The MZIs are the main component, shown as a red structure. A 250 nm thick LPCVD SiO_2 film separates them from the graphene heaters, which consist of Pd/Ti contacts, graphene layer, Al_2O_3 encapsulation, and vias to contact them with an external voltage source. The Sb_2Se_3 PCMs are located on top of the Al_2O_3, protected from oxidation by a ZnS:SiO_2 layer. (b) Microscope image of the PIC consisting of an MZI with a graphene heater and a Sb_2Se_3 square. The electrodes appear blue under the microscope when they are covered with Al_2O_3 and gray where the vias open the encapsulation. The white dotted lines outline the graphene areas. The graphene and Sb_2Se_3 were placed on the second MZI arm to balance potential optical losses due to the graphene and Sb_2Se_3.

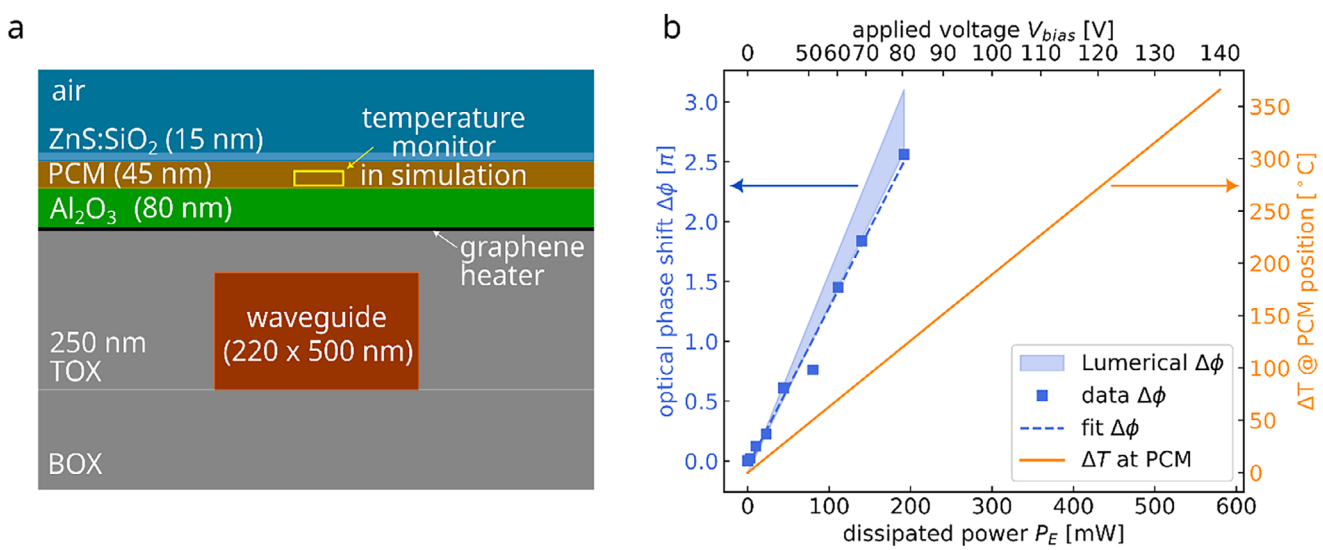

FIGURE 2 | (a) Device model in Lumerical HEAT with a temperature monitor at the position of the PCM. We simulated the device also with Lumerical FDE to check the evanescent field overlap with the PCM, see SI. It yielded an integrated total overlap of the field with the PCM of about 4%. (b) Measured optical phase shift $\Delta\varphi$ as a function of dissipated electrical power P_E of the heater (blue squares) together with a linear fit to the data (blue dashed line). $\Delta\varphi$ was also simulated using Lumerical HEAT + FDE (blue shadow area). Moreover, the simulated temperature at the position of the PCM is shown (solid orange line).

area) match well, with the experimental data providing a lower bound due to the uncertainty in contact resistance. Based on these data and simulations, we are confident that the temperature T at the position of the PCM is predicted by Lumerical HEAT sufficiently well (Figure 2b, orange line). The simulations show that we can reach sufficiently high temperatures at the PCM position, e.g., we can obtain approximately 200°C at a dissipated power of 300 mW, which is in line with reported crystallization temperatures of Sb_2Se_3 amorphous powder and thin films between 180 C and 210°C at standard heating rates (20 K/min) [46–49].

3 | Results and Discussion

We first tested the general capability of our graphene microheaters to switch the phase of Sb_2Se_3 on a substrate without photonic components. We applied a range of bias voltages, V_{bias}, across the heater over an extended period. The voltage and time evolution, along with its impact on the morphology of the PCM, are shown in the set of images in Figure 3a. At V_{bias} = 80 V, the dissipated power corresponds to approximately P_E = 190 mW. Here, no crystallization occurred (Figure 3a1). This was confirmed by our simulations, which predicted a temperature of

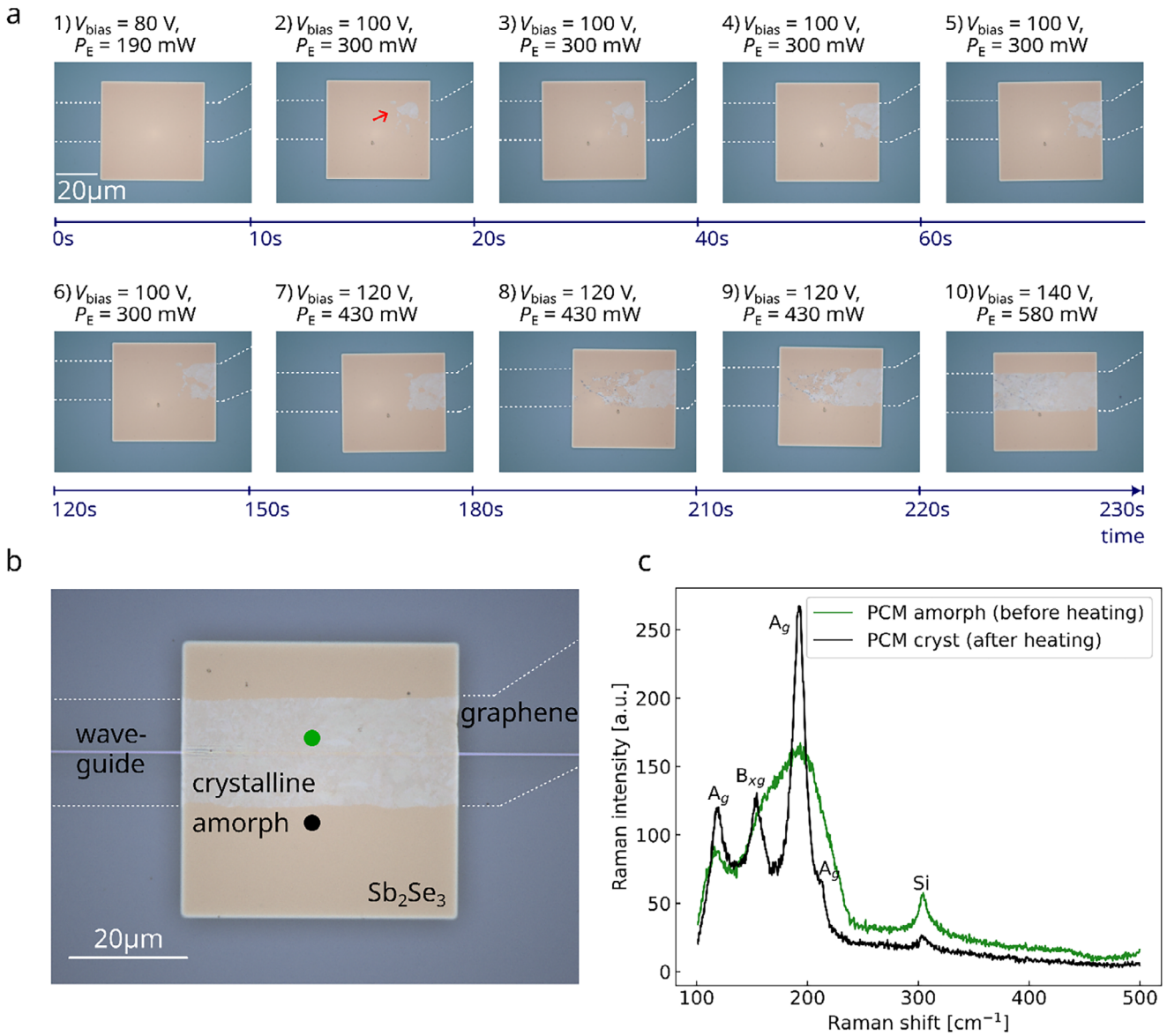

FIGURE 3 | PCM characterization. (a) Microscope images: Successive crystallization of Sb_2Se_3 as a function of the bias voltage V_{bias} applied to the heater. The graphene heater is indicated by the white dotted line. The red arrow in 2) shows the crystallized spot. (b) Crystallized Sb_2Se_3 above the graphene heater on a waveguide. The crystal phase (green spot) of the Sb_2Se_3 has a different appearance under the microscope than the amorphous phase (black spot). (c) Raman spectra of the amorphous (black) and crystallized (green) PCM taken at the spots indicated in (b).

T = 120°C at the PCM at a power of P_E = 190 mW, which is insufficient for crystallization. When V_{bias} was increased to 100 V, corresponding to a P_E of 300 mW, crystallization began within 10 s. This is indicated by the small gray spot in Figure 3a1). We continued to apply 300 mW, and further crystallization was observed until it stopped after a certain time (here: 60 s, Figure 3a4). We then increased V_{bias}, to 120 V, corresponding to a P_E of 430 mW and a temperature of approximately 270°C. This led to more crystallization, albeit still incomplete. When we finally increased V_{bias} to 140 V (P_E = 580 mW), and the temperature to approximately T = 360°C, complete crystallization of the PCM above the graphene heater was achieved (Figure 3a10). We attributed this non-uniform crystallization process to two main sources. On the one hand, the CVD graphene used in this work can exhibit mechanical damage (cracks or holes) from the growth and from the transfer process that can lead to an inhomogeneous heating process across the heater. On the other hand, Se-based phase change materials are known to exhibit growth-driven rather than nucleation-driven crystallization [24, 50]. In this mechanism, once a crystalline nucleus forms at a particular location, crystal growth propagates outward from that point [24, 50]. This inherently stochastic process leads to spatially heterogeneous crystallization fronts and thus contributed to the overall non-uniformity observed in our devices.

We tested the process with the PCM and the graphene heater above a silicon waveguide, as shown in Figure 3b. Here, the morphology change of the PCM on top of the graphene after heating is clearly identifiable by its color change. Additionally, we performed Raman spectroscopy on the PCM of this sample. Figure 3c shows the Raman spectra obtained on the PCM above and next to the graphene heater (green and black dots

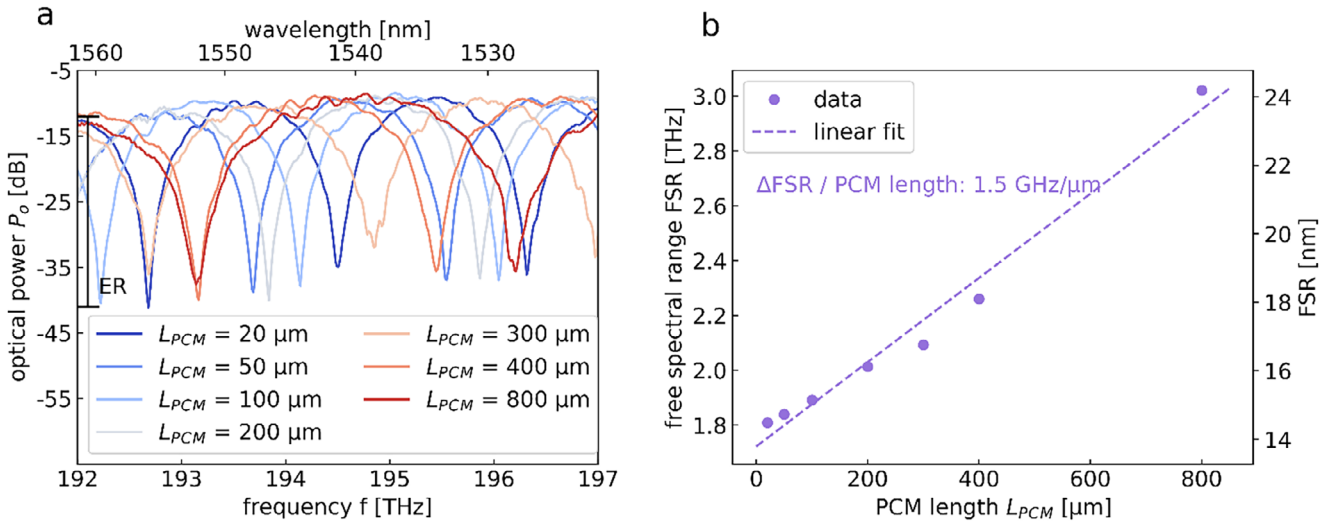

FIGURE 4 | MZI performance dependence on PCM length. (a) Transmission spectra of the MZIs for various PCM lengths L_{PCM}. ER: Extinction ratio. (b) The measured free spectral range FSR in each transmission spectrum as a function of the PCM length L_{PCM} (dashed line: linear fit).

in Figure 3b, respectively). The amorphous Sb_2Se_3 next to the graphene heater showed the broad peak from the Sb_2Se_3 at around 191 cm^{-1} and the silicon peak from the substrate at around 303 cm^{-1}. After crystallization on top of the graphene heater, the three A_g-symmetry peaks appeared at 118, 191, and 212 cm^{-1} and the two B_{xg} peaks at 151 and 153 cm^{-1} which were difficult to resolve. The silicon peak had a reduced height due to a reduced transparency of the crystalline Sb_2Se_3. Our observations were similar to reported values in literature [25, 51–53]. Furthermore, we characterized the graphene heater before and after heating and showed the results in the SI Figure S2 and characterized the cross-over from amorphous and crystallized PCM in a spatially resolved Raman map, the SI Figure S3.

Finally, we note that the slow observed crystallization kinetics of Sb_2Se_3 compared with those of Te-based phase change materials, such as GST, are consistent with the literature [24, 50, 54]. They can be attributed to several key factors. First, the covalent bonding nature of Sb_2Se_3 results in strong directional bonds that require significant energy to break, thereby slowing atomic rearrangement during crystallization. In contrast, GSTs exhibit metavalent bonding, which allows for greater atomic mobility and faster transitions. Second, the structural rigidity introduced by selenium leads to increased bond strength and local distortions that further limit crystallization dynamics. These factors combine to create higher energy barriers for creating stable crystal nuclei in sulfur- and selenium-based PCMs [54, 55].

Next, the effect of the PCM on the optical waveguide mode was studied. For this purpose, we fabricated MZIs and deposited amorphous PCMs on one of their arms. The MZIs had varying lengths of L_{PCM} = 20, 50, 100, 200, 300, 400, and 800 µm and fixed widths of w_{PCM} = 50 µm. The transmission spectra of each MZI were then recorded to extract the free spectral range (FSR), see Figure 4a. The extracted FSRs are plotted as a function of the L_{PCM} in Figure 4b. We use a linear fit for approximation and obtained a slope of 1.5 GHz per micrometer PCM. The change in the FSR due to the PCM originates from a difference in the effective refractive indices of both MZI waveguide arms with and without the PCM. Furthermore, the PCMs of different lengths L_{PCM} had a negligible effect on the extinction ratio, ER, which was approximately 28 dB for all L_{PCM}s (Figure 4a).

Finally, MZI switches with a graphene heater with L_{Graph} = 90 µm and w_{Graph} = 20 µm and with a PCM patch of L_{PCM} = w_{PCM} = 50 µm were studied (see microscope image in Figure 1b). We recorded the MZI transmission spectrum after applying an increasing voltage V_{bias} to the graphene heater to approach crystallization of the PCM as established in Figure 3. We expected a continuous shift in the spectrum upon switching the PCM in one arm of the MZI, as this causes a significant shift in the refractive index. The V_{bias} steps are plotted as a function of time in Figure 5a. After each step, V_{bias} was set to 0 V to measure the spectrum of the MZI. Thus, we ensured that the measured phase shift was caused by the crystallization of PCM and did not originate from heating. Figure 5b shows the corresponding transmission spectra of the MZI and their shifts due to successive crystallization. We used the minima of the transmission spectra, expressed in units of π, and plotted them as a function of V_{bias} in Figure 5c to quantify the phase shifts. We observed no phase shift for V_{bias} up to 100 V, which is where crystallization began in our preliminary experiment (Figure 3). Crystallization started at 110 V, indicated by an initial phase shift of 0.1 π. We then held the voltage at 110 V for 150 s and measured the phase shift every 30 s. The phase shift increased with time and started to saturate, similar to the observations in Figure 3a. Few then increased V_{bias} to 120 and 130 V where the PCM completely crystallized. A microscope image of the completely crystallized PCM is shown in the inset of Figure 5c. The data in Figure 5 generally confirm the crystallization process as observed in Figure 3. However, there is a slight deviation of approximately 7%, which we attribute to variations in the contact and sheet resistances of the graphene heater and the resulting inhomogeneity in the heating process. We achieved a maximum phase shift of approximately $\Delta\varphi = 0.7\,\pi$ with $V_\pi L \approx 0.56$ Vcm and a slope of 0.014 π/µm PCM.

We compared our results with experimental demonstrations of non-volatile photonic devices based on phase change materials

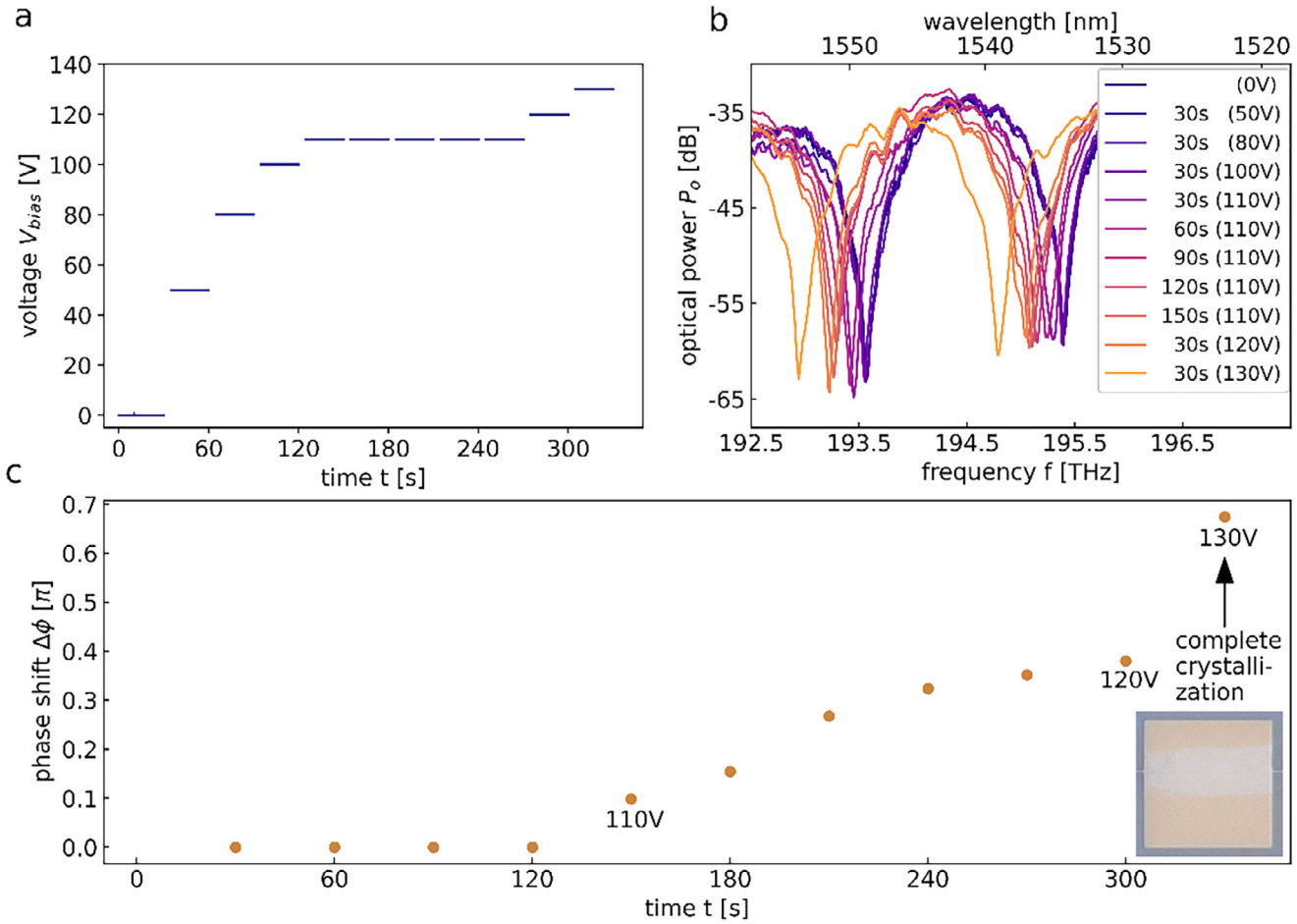

FIGURE 5 | Non-volatile MZI tuning by crystallizing the PCM with the graphene heater. (a) Applied voltage V_{bias} to the graphene as a function of time. After applying each voltage for 30 s, V_{bias} was set to 0 V and the spectrum was measured (see Figure 5b) to determine the phase shift due to crystallized PCM (see Figure 5c). Thus, avoiding effects from heating in the measured phase shift. (b) Transmission spectra of an MZI with graphene heater of dimensions L_{Graph} = 90 µm and w_{Graph} = 20 µm and PCM of dimensions $L_{PCM} = w_{PCM}$ = 50 µm. The PCM is partially switched to the crystalline state with the graphene heater that led to a phase shift $\Delta\varphi$ in the transmission spectrum. (c) Measured phase shift $\Delta\varphi$ due to crystallized PCM as a function of time. The data points were taken after applying the corresponding voltage V_{bias} as shown in Figure 5a. The voltage V_{bias} was set to 0 V during the measurement of the spectra to deduce the phase shift. At V_{bias} = 130 V, the PCM is completely crystallized, see inset.

in the literature (Table 1). Many implementations with various PCMs (GST, Sb_2S_3 and Sb_2Se_3) utilized doped silicon heaters to switch the PCM. They achieved maximum phase shifts of 0.3 π to 1 π, and moderate extinction ratios between 10 and 20 dB. Ríos et al. [27] achieved an extinction ratio of ER = 35 dB in an MZI with Sb_2Se_3. However, doped silicon heaters require ion implantation and annealing, which cannot be used in future electronic–photonic systems integrated on advanced silicon logic chips because their processing temperatures are incompatible with maximum BEOL temperatures of approximately 400°C. In contrast, graphene heaters can be fabricated far below the maximum BEOL temperatures. Micro ring resonators with graphene heaters for Sb_2Se_3 showed reversible switching and a maximum phase shift of 0.008 π with a voltage-length product of $V_\pi L$ = 0.496 V cm [30]. Our MZIs with graphene heaters achieved switching from the amorphous to the crystalline phase of Sb_2Se_3, resulting in a maximum phase shift of $\Delta\varphi = 0.7\,\pi$. We achieved full crystallization with a phase shift of $\Delta\varphi = 0.7\,\pi$ at a voltage of 130 V within a rather long crystallization time of 30 s. We did not measure shorter times because we wanted to determine the maximum phase shift after complete crystallization. However, according to literature, shorter times should be possible. Moreover, switching was not reversible and the required power and applied voltage of 130 V was very high. This is because our device was not mainly optimized for low operation voltage. The main reason for that is the thick 80 nm Al_2O_3 layer that separated the graphene from the PCM. In previous realizations, the PCM was either separated from the graphene by only a very thin Al_2O_3 layer, see Ref [56], or directly deposited on the photonic structure, see Ref [21]. This can increase the efficiency of the heat transfer from the heat source to the PCM but, in case of graphene, it might come along with a decreasing long-term stability of the graphene due to adsorbates and charge traps from the ambience and from next lithography steps [57, 58], see the discussion in the SI. A second important reason for the high-power consumption and high necessary voltage of the presented device is the high contact resistance which leads to dissipation of 40% of the total power at the contacts and cannot be used for heating the PCM. Sandwich or edge contacts might be an alternative to the use of bottom contacts and it was shown that the former exhibit indeed a lower contact resistance, see ref [59]. Advantageously, the large achieved tuning range of 0.7 π is suitable for switches with random initial phases

TABLE 1 | Recently, demonstrated non-volatile photonic devices based on phase change materials. DC: directional coupler. MRR: micro ring resonator. RR: racetrack resonator. DS: doped silicon.

Work (year)	Device	PCM	Heater (switching energy)	Reverse switching	ER (dB)	Shift (π/ µm PCM)	Total shift
Chen et al. [13]. (2022)	DC	GST	DS (0.5 µJ)	Yes	8	—	—
Zheng et al. [15]. (2020)	MRR	GST	DS (10 mW)	Yes	15	—	—
Faneca et al. [60]. (2020)	MZI	GST	Oven	No	12	—	$\approx 1\pi$
Faneca et al. [61]. (2020)	MZI	GST	oven	No	12	—	—
Chen et al. [21]. (2023)	MRR	Sb_2S_3	DS (10.2 mJ)	Yes	10	0.03	0.3π
Ilie et al. [62]. (2022)	RR	Sb_2S_3	Laser	No	18	—	3.3π
Ríos et al. [27]. (2022)	MRR	Sb_2Se_3	DS	yes	15	0.09	0.28π
Ríos et al. [27]. (2022)	MZI	Sb_2Se_3	DS (38.4 µJ)	Yes	35	0.16	$\approx 1\pi$
Fang et al. [28]. (2024)	RR	Sb_2Se_3	DS (5.4 mJ)	Yes	10	—	—
Faneca et al. [63]. (2021)	MZI	Sb_2S3, Sb_2Se_3	—	no	20	—	$>1\pi$
Fang et al. [30]. (2022)	MRR	Sb_2Se_3	Graphene (9.25 nJ)	Yes	4	0.0014	0.008π
This work	MZI	Sb_2Se_3	Graphene (5.8J)	No	28	0.014	0.7π

whose output needs to be set arbitrarily between minimum and full output power and for applications like photonic computing where it is important to set values between "close to zero" and one. Finally, the switch has a voltage-length product $V_\pi L \approx$ 0.56 Vcm. This is a standard measure for characterizing thermo-optical phase shifters. For non-volatile switches based on phase change material, we used the voltage for switching the PCM's phase and the PCM length for a π-shift as performed in Ref [27]. This gives 130 V • 0.6 • 0.005 cm / 0.7 = 0.56 Vcm for our switch comparable to previous realizations in Ref [30] with 0.49 Vcm. We note that we follow Ref [30] and exclude the power loss due to the contact resistance of 40% that gives the factor of 0.6 in our calculation.

4 | Conclusions

A non-volatile Mach-Zehnder switch based on the phase change material Sb_2Se_3 and integrated graphene heaters was demonstrated. We observed large phase shifts of $\Delta\varphi = 0.7\ \pi$ with $V_\pi L \approx$ 0.56 Vcm, and an extinction ratio of 28 dB. The Sb_2Se_3 was gradually crystallized with the graphene microheater, enabling controllably tuning of the MZI output. Furthermore, we used a wafer scale process for the fabricated non-volatile switches allowing for scalability. With that, the study sets the stage for future optimization and investigation of reliability and tuning of the non-volatile switch. One way for optimizing is to reduce the relatively thick separation layer between graphene and PCM. To simultaneously protect and ensure reliability of the graphene in long-term, see ref [57, 58], one can use a thick Al_2O_3 encapsulation above the graphene and etch it down in the region of the PCM, thus, requiring one more lithography and etching step. A second optimization is to reduce the heater width (see Figure S6 in the Appendix) or contact resistance (see Ref [42, 64, 65].) and, hence, make the graphene heaters more efficient. These parameters are critical for the use of the switch in emerging applications like photonic networks, optical memory, filters with permanent trimming or optical FPGAs.

Author Contributions

J.S. designed the layout. **J.S.**, **H.L.**, **B.C.**, **F.H.**, **T.V.**, **M.O.**, **C.P.**, and **B.C**h. fabricated the device. **J.S.** performed the electro-optical measurements for data acquisition. **J.S.** worked on data evaluation. **M.L.** and **M.W.** acquired funding. **J.S.** wrote the manuscript. All the authors revised and cowrote the manuscript.

Acknowledgements

The authors thank Jens Bolten, Michael Möller and Lisa Ehlert for careful sample preparation for electron beam lithography. This project was funded by the German Federal Ministry of Education and Research (BMFTR) under the NeuroSys Cluster4Future project B with grant 03ZU1106BB and the NeuroSys project B.2 with grant 03ZU2106FA and 03ZU2106BA.

Open access funding enabled and organized by Projekt DEAL.

Conflicts of Interest

The authors declare no conflicts of interest.

Data Availability Statement

The data that support the findings of this study are available from the corresponding author upon reasonable request.

References

1. M. S. Nisar, X. Yang, L. Lu, J. Chen, and L. Zhou, "On-Chip Integrated Photonic Devices Based on Phase Change Materials," *Photonics* 8, no. 6 (2021): 205, https://doi.org/10.3390/photonics8060205.

2. M. Wuttig, H. Bhaskaran, and T. Taubner, "Phase-Change Materials for Non-Volatile Photonic Applications," *Nature Photonics* 11, no. 8 (2017): 465–476, https://doi.org/10.1038/nphoton.2017.126.

3. S. Abdollahramezani, O. Hemmatyar, H. Taghinejad, et al., "Tunable Nanophotonics Enabled by Chalcogenide Phase-Change Materials," *Nanophotonics* 9, no. 5 (2020): 1189–1241, https://doi.org/10.1515/nanoph-2020-0039.

4. R. Chen, Z. Fang, F. Miller, H. Rarick, J. E. Fröch, and A. Majumdar, "Opportunities and Challenges for Large-Scale Phase-Change Material Integrated Electro-Photonics," *ACS Photonics* 9, no. 10 (2022): 3181–3195, https://doi.org/10.1021/acsphotonics.2c00976.

5. H. Zhou, J. Dong, J. Cheng, et al., "Photonic Matrix Multiplication Lights up Photonic Accelerator and Beyond," *Light: Science & Applications* 11, no. 1 (2022): 30, https://doi.org/10.1038/s41377-022-00717-8.

6. J. Cheng, H. Zhou, and J. Dong, "J. Photonic Matrix Computing: From Fundamentals to Applications," *Nanomaterials* 11, no. 7 (2021): 1683, https://doi.org/10.3390/nano11071683.

7. Q. Zhang, H. Yu, M. Barbiero, B. Wang, and M. Gu, "Artificial Neural Networks Enabled by Nanophotonics," *Light Science & Application* 8, no. 1 (2019): 42, https://doi.org/10.1038/s41377-019-0151-0.

8. Y. Shen, N. C. Harris, S. Skirlo, et al., "Deep Learning With Coherent Nanophotonic Circuits," *Nature Photonics* 11, no. 7 (2017): 441–446, https://doi.org/10.1038/nphoton.2017.93.

9. W. Zhou, N. Farmakidis, J. Feldmann, et al., "Phase-Change Materials for Energy-Efficient Photonic Memory and Computing," *MRS Bulletin* 47, no. 5 (2022): 502–510, https://doi.org/10.1557/s43577-022-00358-7.

10. P. Guo, S. Yu, W. Hou, and L. Guo, "Phase-Change Material-Assisted All-Optical Temporal Differentiator," *Optics Express* 31, no. 3 (2023): 4306, https://doi.org/10.1364/OE.475047.

11. W. Bogaerts, D. Pérez, J. Capmany, et al., "Programmable Photonic Circuits," *Nature* 586, no. 7828 (2020): 207–216, https://doi.org/10.1038/s41586-020-2764-0.

12. R. Chen, V. Tara, J. Dutta, Z. Fang, J. Zheng, and A. Majumdar, "Low-Loss Multilevel Operation Using Lossy Phase-Change Material-Integrated Silicon Photonics," *Journal of Optical Microsystems* 4, no. 03 (2024): 031202, https://doi.org/10.1117/1.JOM.4.3.031202.

13. R. Chen, Z. Fang, J. E. Fröch, P. Xu, J. Zheng, and A. Majumdar, "Broadband Nonvolatile Electrically Controlled Programmable Units in Silicon Photonics," *ACS Photonics* 9, no. 6 (2022): 2142–2150, https://doi.org/10.1021/acsphotonics.2c00452.

14. J. Faneca, S. Meyer, F. Y. Gardes, and D. N. Chigrin, "Graphene Microheater for Phase Change Chalcogenides Based Integrated Photonic Components," *Optical Materials Express* 12, no. 5 (2022): 1991, https://doi.org/10.1364/OME.452153.

15. J. Zheng, Z. Fang, C. Wu, et al., "Nonvolatile Electrically Reconfigurable Integrated Photonic Switch Enabled by a Silicon PIN Diode Heater," *Advanced Materials* 32, no. 31 (2020): 2001218, https://doi.org/10.1002/adma.202001218.

16. J.-H. Chen, S.-K. Chiu, J.-D. Luo, et al., "Robust Formation of Amorphous Sb_2S_3 on Functionalized Graphene for High-Performance Optoelectronic Devices in the Cyan-Gap," *Scientific Reports* 10, no. 1 (2020): 14873, https://doi.org/10.1038/s41598-020-70879-1.

17. Z. Cui, K. Bu, Y. Zhuang, et al., "Phase Transition Mechanism and Bandgap Engineering of Sb_2S_3 at Gigapascal Pressures," *Communications Chemistry* 4, no. 1 (2021): 125, https://doi.org/10.1038/s42004-021-00565-4.

18. C. Liu, Y. Yuan, L. Cheng, et al., "A Study on Optical Properties of Sb_2Se_3 Thin Films and Resistive Switching Behavior in Ag/Sb_2Se_3/W Heterojunctions," *Results in Physics* 13 (2019): 102228, https://doi.org/10.1016/j.rinp.2019.102228.

19. Y. Gutiérrez, A. P. Ovvyan, G. Santos, et al., "Interlaboratory Study on Sb_2S_3 Interplay Between Structure, Dielectric Function, and Amorphous-to-Crystalline Phase Change for Photonics," *Iscience* 25, no. 6 (2022): 104377, https://doi.org/10.1016/j.isci.2022.104377.

20. A. Biegański, M. Perestjuk, R. Armand, et al., "Sb_2S_3 as a Low-Loss Phase-Change Material for Mid-IR Photonics," *Opt Mater Express* 14, no. 4 (2024): 862, https://doi.org/10.1364/OME.511923.

21. R. Chen, Z. Fang, C. Perez, et al., "Non-Volatile Electrically Programmable Integrated Photonics With a 5-Bit Operation," *Nature Communications* 14, no. 1 (2023): 3465, https://doi.org/10.1038/s41467-023-39180-3.

22. Z. Fang, J. Zheng, A. Saxena, J. Whitehead, Y. Chen, and A. Majumdar, "Non-Volatile Reconfigurable Integrated Photonics Enabled by Broadband Low-Loss Phase Change Material," *Advanced Optical Materials* 9, no. 9 (2021): 2002049, https://doi.org/10.1002/adom.202002049.

23. D. Lawson, S. Blundell, M. Ebert, O. L. Muskens, and I. Zeimpekis, "Optical Switching Beyond a Million Cycles of Low-Loss Phase Change Material Sb_2 Se_3," *Optical Materials Express* 14, no. 1 (2024): 22, https://doi.org/10.1364/OME.509434.

24. M. J. Müller, A. Yadav, C. Persch, S. Wahl, F. Hoff, and M. Wuttig, "Tailoring Crystallization Kinetics of Chalcogenides for Photonic Applications," *Advanced Electronic Materials* 8, no. 8 (2022): 2100974, https://doi.org/10.1002/aelm.202100974.

25. M. Delaney, I. Zeimpekis, D. Lawson, D. W. Hewak, and O. L. Muskens, "A New Family of Ultralow Loss Reversible Phase-Change Materials for Photonic Integrated Circuits: Sb_2S_3 and Sb_2Se_3," *Advanced Functional Materials* 30, no. 36 (2020): 2002447, https://doi.org/10.1002/adfm.202002447.

26. M. Delaney, I. Zeimpekis, H. Du, et al., "Nonvolatile Programmable Silicon Photonics Using an Ultralow-Loss Sb_2 Se_3 Phase Change Material," *Science Advances* 7, no. 25 (2021): abg3500, https://doi.org/10.1126/sciadv.abg3500.

27. C. Ríos, Q. Du, Y. Zhang, et al., "Ultra-Compact Nonvolatile Phase Shifter Based on Electrically Reprogrammable Transparent Phase Change Materials," *PhotoniX* 3, no. 1 (2022): 26, https://doi.org/10.1186/s43074-022-00070-4.

28. Z. Fang, B. Mills, R. Chen, et al., "Arbitrary Programming of Racetrack Resonators Using Low-Loss Phase-Change Material Sb_2 Se_3," *Nano Letters* 24, no. 1 (2024): 97–103, https://doi.org/10.1021/acs.nanolett.3c03353.

29. C. Ríos, Y. Zhang, M. Y. Shalaginov, et al., "Multi-Level Electro-Thermal Switching of Optical Phase-Change Materials Using Graphene," *Advanced Photonics Research* 2, no. 1 (2021): 2000034, https://doi.org/10.1002/adpr.202000034.

30. Z. Fang, R. Chen, J. Zheng, et al., "Ultra-Low-Energy Programmable Non-Volatile Silicon Photonics Based on Phase-Change Materials With Graphene Heaters," *Nature Nanotechnology* 17, no. 8 (2022): 842–848, https://doi.org/10.1038/s41565-022-01153-w.

31. D. Schall, M. Mohsin, A. A. Sagade, et al., "Infrared Transparent Graphene Heater for Silicon Photonic Integrated Circuits," *Optics Express* 24, no. 8 (2016): 7871, https://doi.org/10.1364/OE.24.007871.

32. N. Negm, S. Zayouna, S. Parhizkar, et al., "Graphene Thermal Infrared Emitters Integrated Into Silicon Photonic Waveguides," *ACS Photonics* 11, no. 8 (2024): 2961–2969, https://doi.org/10.1021/acsphotonics.3c01892.

33. J. Samland, B. Canto, M. Otto, et al., "Graphene Heaters for Tunable Mach–Zehnder Interferometers in Silicon Photonics at the C-Band Wavelength," .

34. K. W. Clark, X.-G. Zhang, I. V. Vlassiouk, G. He, R. M. Feenstra, and A.-P. Li, "Spatially Resolved Mapping of Electrical Conductivity Across Individual Domain (Grain) Boundaries in Graphene," *ACS Nano* 7, no. 9 (2013): 7956–7966, https://doi.org/10.1021/nn403056k.

35. W. Zhu, T. Low, V. Perebeinos, et al., "Structure and Electronic Transport in Graphene Wrinkles," *Nano Letters* 12, no. 7 (2012): 3431–3436, https://doi.org/10.1021/nl300563h.

36. M. A. Ghani, S. Sarkar, J.-I. Lee, et al., "Metal Films on Two-Dimensional Materials: Van Der Waals Contacts and Raman Enhancement," *ACS Applied Materials & Interfaces* 16, no. 6 (2024): 7399–7405, https://doi.org/10.1021/acsami.3c15598.

37. M. Chhowalla, D. Jena, and H. Zhang, "Two-Dimensional Semiconductors for Transistors," *Nature Reviews Materials* 1, no. 11 (2016): 16052, https://doi.org/10.1038/natrevmats.2016.52.

38. P. Blake, R. Yang, S. V. Morozov, et al., "Influence of Metal Contacts and Charge Inhomogeneity on Transport Properties of Graphene near the Neutrality Point," *Solid State Communications* 149 (2009): 1068–1071, https://doi.org/10.1016/j.ssc.2009.02.039%2520Get%2520rights%2520and%2520content.

39. F. Xia, V. Perebeinos, Y. Lin, Y. Wu, and P. Avouris, "The Origins and Limits of Metal–graphene Junction Resistance," *Nature Nanotechnology* 6, no. 3 (2011): 179–184, https://doi.org/10.1038/nnano.2011.6.

40. R. Nouchi, T. Saito, and K. Tanigaki, "Observation of Negative Contact Resistances in Graphene Field-Effect Transistors," *Journal of Applied Physics* 111, no. 8 (2012): 084314, https://doi.org/10.1063/1.4705367.

41. S. Venica, F. Driussi, A. Gahoi, P. Palestri, M. C. Lemme, and L. Selmi, "On the Adequacy of the Transmission Line Model to Describe the Graphene–Metal Contact Resistance," *IEEE Transactions on Electron Devices* 65, no. 4 (2018): 1589–1596, https://doi.org/10.1109/TED.2018.2802946.

42. A. Gahoi, S. Wagner, A. Bablich, S. Kataria, V. Passi, and M. C. Lemme, "Contact Resistance Study of Various Metal Electrodes With CVD Graphene," *Solid-State Electronics* 125 (2016): 234–239.

43. T. Cusati, G. Fiori, A. Gahoi, et al., "Electrical Properties of Graphene-Metal Contacts," *Scientific Reports* 7, no. 1 (2017): 1–11, https://doi.org/10.1038/s41598-017-05069-7.

44. A. Gahoi, S. Kataria, F. Driussi, et al., "Dependable Contact Related Parameter Extraction in Graphene–Metal Junctions," *Advanced Electronic Materials* 6 (2020): 2000386, https://doi.org/10.1002/aelm.202000386.

45. F. Driussi, S. Venica, A. Gahoi, S. Kataria, M. C. Lemme, and P. Palestri, "Dependability Assessment of Transfer Length Method to Extract the Metal–Graphene Contact Resistance," *IEEE Transactions on Semiconductor Manufacturing* (2020): 1–1, https://doi.org/10.1109/TSM.2020.2981199.

46. K. Zhang, Y. Li, Q. Huang, et al., "Ultrastable Amorphous Sb_2 Se_3 Film," *The Journal of Physical Chemistry B* 121, no. 34 (2017): 8188–8194, https://doi.org/10.1021/acs.jpcb.7b03408.

47. J. Pries, "Interplay of glass dynamics and crystallization kinetics in amorphous phase change materials," .

48. S. Raoux, J. L. Jordan-Sweet, and A. J. Kellock, "Crystallization Properties of Ultrathin Phase Change Films," *Journal of Applied Physics* 103, no. 11 (2008): 114310, https://doi.org/10.1063/1.2938076.

49. B. J. Kooi and M. Wuttig, "Chalcogenides by Design: Functionality Through Metavalent Bonding and Confinement," *Advanced Materials* 32, no. 21 (2020): 1908302, https://doi.org/10.1002/adma.201908302.

50. M. J. Müller, C. Morell, P. Kerres, et al., "Decoupling Nucleation and Growth in Fast Crystallization of Phase Change Materials," *Advanced Functional Materials* 34, no. 39 (2024): 2403476, https://doi.org/10.1002/adfm.202403476.

51. A. Shongalova, M. R. Correia, B. Vermang, J. M. V. Cunha, P. M. P. Salomé, and P. A. Fernandes, "On the Identification of Sb_2Se_3 Using Raman Scattering," *MRS Communications* 8, no. 3 (2018): 865–870, https://doi.org/10.1557/mrc.2018.94.

52. P. Vidal-Fuentes, M. Guc, X. Alcobe, et al., "Multiwavelength excitation Raman scattering study of Sb_2Se_3 Compound: Fundamental Vibrational Properties and Secondary Phases Detection," *2D Materials* 6 (2019): 045054, https://doi.org/10.1088/2053-1583/ab4029.

53. A. Shongalova, M. R. Correia, J. P. Teixeira, et al., "Growth of Sb_2Se_3 Thin Films by Selenization of RF Sputtered Binary Precursors," *Solar Energy Materials and Solar Cells* 187 (2018): 219–226, https://doi.org/10.1016/j.solmat.2018.08.003.

54. F. Hoff, J. Pries, J. Köttgen, P. Lucas, and M. Wuttig, "Controlling the Crystallization Kinetics of Low Loss Phase Change Material Sb_2 S_3," *Advanced Physics Research* 4 (2025): 2500005, https://doi.org/10.1002/apxr.202500005.

55. R. Shekhawat, H. Pamuluri, V. Erkkara Madhavan, and K. Ramesh, "Structural Transformation and Phase Change Properties of Se Substituted GeTe," *Scientific Reports* 11, no. 1 (2021): 7604, https://doi.org/10.1038/s41598-021-87206-x.

56. Z. Fang, R. Chen, J. Zheng, et al., "Ultra-Low-Energy Programmable Non-Volatile Silicon Photonics Based on Phase-Change Materials With Graphene Heaters," *Nature Nanotechnology* 17, no. 8 (2022): 842–848, https://doi.org/10.1038/s41565-022-01153-w.

57. A. A. Sagade, D. Neumaier, D. Schall, et al., "Highly Air Stable Passivation of Graphene Based Field Effect Devices," *Nanoscale* 7, no. 8 (2015): 3558–3564, https://doi.org/10.1039/C4NR07457B.

58. J. A. Alexander-Webber, A. A. Sagade, A. I. Aria, et al., "Encapsulation of Graphene Transistors and Vertical Device Integration by Interface Engineering With Atomic Layer Deposited Oxide," *2D Materials* 4, no. 1 (2016): 011008, https://doi.org/10.1088/2053-1583/4/1/011008.

59. A. D. Franklin, S.-J. Han, A. A. Bol, and V. Perebeinos, "Double Contacts for Improved Performance of Graphene Transistors," *IEEE Electron Device Letters* 33, no. 1 (2012): 17–19, https://doi.org/10.1109/LED.2011.2173154.

60. J. Faneca, T. D. Bucio, F. Y. Gardes, and A. Baldycheva, "O-Band N-Rich Silicon Nitride MZI Based on GST," *Applied Physics Letters* 116, no. 9 (2020): 093502, https://doi.org/10.1063/1.5140350.

61. J. Faneca, S. Garcia-Cuevas Carrillo, E. Gemo, et al., "Performance Characteristics of Phase-Change Integrated Silicon Nitride Photonic Devices in the O and C Telecommunications Bands," *Optical Materials Express* 10, no. 8 (2020): 1778, https://doi.org/10.1364/OME.397833.

62. S. T. Ilie, J. Faneca, I. Zeimpekis, et al., "Thermo-Optic Tuning of Silicon Nitride Microring Resonators With Low Loss Non-Volatile Sb_2S_3 Phase Change Material," *Scientific Reports* 12, no. 1 (2022): 17815, https://doi.org/10.1038/s41598-022-21590-w.

63. J. Faneca, I. Zeimpekis, S. T. Ilie, et al., "Towards Low Loss Non-Volatile Phase Change Materials in Mid Index Waveguides," *Neuromorphic Computing and Engineering* 1, no. 1 (2021): 014004, https://doi.org/10.1088/2634-4386/ac156e.

64. V. Passi, A. Gahoi, E. G. Marin, et al., "Ultralow Specific Contact Resistivity in Metal–Graphene Junctions via Contact Engineering," *Advanced Materials Interfaces* 6, no. 1 (2019): 1801285, https://doi.org/10.1002/admi.201801285.

65. V. Jangra, S. Kataria, and M. C. Lemme, "Reducing the Metal–Graphene Contact Resistance Through Laser-Induced Defects," *ACS Applied Electronic Materials* 6, no. 7 (2024): 4883–4890, https://doi.org/10.1021/acsaelm.4c00305.

Supporting Information

Additional supporting information can be found online in the Supporting Information section.

Supporting File: adom71377-sup-0001-SuppMat.docx.